diffusion-fundamentals

The Open-Access Journal for the Basic Principles of Diffusion Theory, Experiment and Application

NMR Diffusion Diffraction and Diffusion Interference from Cells

Philip W. Kuchel[1], Guilhem Pages[1]

[1] School of Molecular and Microbial Biosciences, University of Sydney, NSW 2006, Australia

Corresponding author:
Philip W. Kuchel
School of Molecular and Microbial Biosciences
University of Sydney
NSW 2006, Australia
E-Mail: p.kuchel@mmb.usyd.edu.au

Abstract

Pulsed field gradient spin-echo (PGSE) NMR spectroscopy is the definitive means for measuring translational motion of molecules in free solution and in heterogeneous systems. A unique 'twist' on the method is that in some systems in which diffusion is restricted the PGSE experiment yields information on the geometrical properties of the confining boundaries. When applied to red blood cells (RBCs) in suspensions, using intense magnetic field gradients (around 10 T m^{-1}), the graph of normalized NMR-signal intensity versus the magnitude of the field gradients has the form of the diffraction and interference patterns that are seen in physical optics. We review here the nature of these so called *q*-space plots and discuss a data-processing method that adds objectivity to estimates of the mean RBC diameter. Convection potentially interferes with the veracity of these measurements so an experiment is reported in which a cell-free sample was deliberately made to flow. The very simple analysis of flow diffraction yielded estimates of flow that were in remarkable agreement with gravimetric measurements. Finally, in a theoretical study using a model of uniformly arrayed octagonal prisms that were 'morphed' in a systematic way, the dependence of the form of *q*-space plots on prism shape and packing density was obtained. This showed that elaborately shaped *q*-space plots can be obtained from simple periodic arrays of 'cells'. The uniqueness or otherwise of shapes of *q*-space plots, and the prospect of generally solving the inverse problem whereby *q*-space analysis yields detailed information on packing arrangements is poised for further detailed investigations.

Keywords: convection; diffusion diffraction; diffusion interference; erythrocyte; flow diffraction; physical optics; *q*-space plot; pulsed field gradient spin-echo; red blood cell; restricted diffusion

Abbreviations: Ht, haematocrits; PGSE, pulsed field gradient spin-echo; RBC, red blood cell; SGP, short gradient pulse.

1. Introduction

The thermally driven random motion of water and solute molecules in cells is a major factor in determining the access of substrates to enzymes that act upon them and hence carry out metabolic processes [1]. Pulsed field gradient spin-echo (PGSE) NMR [2,3] has yielded estimates of the diffusion coefficients in heterogeneous systems using 'classical' methods of data analysis [4,5] that continue to be relevant with modern NMR pulse sequences. The mobility of water [6], low molecular weight solutes including metabolites [7,8], and proteins such as haemoglobin inside the human red blood cell (RBC) [9], have been measured this way. From a knowledge of the apparent diffusion coefficients the microviscosity and mean residence times in tissue compartments and cells have been estimated [10].

Compartmentation of water and solutes between different cells in a tissue, and between organelles within a single cell, is one means whereby metabolic processes are regulated. Changes in cell shape occur naturally and yet the kinetics and energetics of the processes are poorly understood. Such shape changes are exemplified by the autonomous transition of the human RBC from its usual biconcave-disc shape, to an 'early' echinocyte (Greek, *echinos* = sea urchin) that has ~20 rounded projections, then to a 'late' echinocyte that has sharp membranous spikes, finally to a spherocyte, that has few membranous protrusions, with a total volume that is ~75% of the original value. Under the appropriate conditions of zero glucose concentration, the first shape transition takes ~5 min, while the later stages evolve over 20 h [e.g., 11,12]. Experimental delineation of cell shape in concentrated suspensions of RBCs such as those encountered in the blood are not available by conventional light microscopy; but PGSE NMR can uniquely provide estimates of cell dimensions by exploiting signals from molecules that undergo restricted diffusion [13-16]. It is this aspect of PGSE NMR that we focus on in this paper via the following four related topics.

2. q-Space of RBCs

For a solute in an isotropic medium undergoing unbounded diffusion a plot of the natural logarithm of the PGSE NMR signal intensity versus the square of the amplitude of the magnetic field gradients is a straight line. The negative slope of this so called Stejskal-Tanner plot is proportional to the diffusion coefficient of the solute [2,3]. Or, a plot of the intensity versus g (not g^2) is a smooth monotonically-strictly-decreasing half-

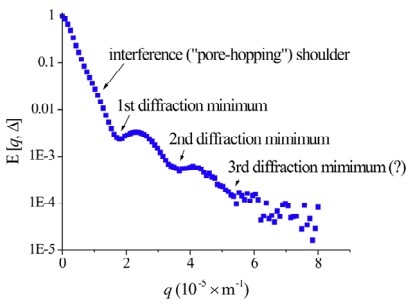

Fig. 1. ^{1}H NMR q-space plot derived from the ^1H_2O signal at 400 MHz from water in a ~1 mL suspension of human RBCs (haematocrit, volume fraction that was cells ~70%) at 25°C in a 10-mm NMR tube. E[q, Δ] is the spin-echo PGSE NMR signal intensity relative to the value obtained when the magnetic field gradients, g = 0; the gradients were in the direction of the main magnetic field $\mathbf{B}_0$ and had a maximum value of 9.4 T m^{-1}. $q = (1/2\pi)\,\gamma\,g\delta$, where γ is the magnetogyric ratio; and δ is the pulse duration in the PGSE experiment. Annotation highlights key features. (Adapted from [16].)

Gaussian shape. On the other hand if diffusion is restricted in the sample the latter curve is no longer simple. In an extreme case, with a highly ordered sample the outcome is like that seen in Fig. 1; this shows a typical *q*-space plot obtained from the ^1H_2O signal from a suspension of human RBCs.

The main features evident in Fig. 1 are manifestations of what is called *q*-space diffusion-diffraction [2] but there is an additional minor but very reproducible feature [11,12,16,17] from what is called diffusion interference; it is so named because it arises from diffusion *between* the RBCs and is similar to the situation seen with two- or multi-slit interference in physical optics [2, 18]. The diffraction effect arises from water that diffuses in a constricted way inside the cells and consequently produces an effect like that for diffraction of light through a single slit [18], i.e., a signal of squared sinc-function shape (see below).

It is worth emphasizing that while *q*-space plots have been reported from other samples, both biological and inanimate ones, none to our knowledge show the same high level of structural features with up to four maxima in the curves. This favourable outcome is ascribed to the precise size discrimination that occurs in the production of RBCs in the mammalian bone marrow; thus the cells as particles have a very narrow size distribution. Furthermore, the biconcave-discs become aligned in the magnetic field of the NMR spectrometer, $\mathbf{B}_0$, with their flattish faces parallel to it thus constituting a very ordered system [17,19].

The mechanism of the alignment does not reside with paramagnetic haemoglobin, as is often supposed; it even occurs when the cells are saturated with oxygen or carbon monoxide that renders the iron in the heme of haemoglobin low-spin FeII and diamagnetic. The effect is due to the diamagnetic anisotropy of the phospholipids in the RBC plasma membranes for which the minimum-energy orientation is perpendicular to $\mathbf{B}_0$; the maximum number of phospholipid-fatty acid chains are aligned at right angles to $\mathbf{B}_0$ when the disc-planes of the RBCs are parallel to $\mathbf{B}_0$. Thus, *q*-space data can be used to estimate the mean diameter of the RBCs in the sample [17].

For cylinders lying across the direction of the field-gradient the mean cell diameter is given by $1.22/ q_{min}$, where q_{min} is the value of q at the first diffraction minimum of the plot [17]. Although the human RBC has the shape of a biconcave disc, it is closely approximated by a short cylinder of main diameter ~6-8 μm.

3. Feature Enhancement

Kärger et al. [20,21] proposed the idea, and then in studies of yeast cells, Cory and Garroway [13] emphasized that an inverse Fourier relationship exists between q and the mean displacement, $\bar{z}$, of the molecules moving during the 'diffusion time' Δ of the PGSE experiment (see Eq. 6 below). Thus Fourier transformation of the spin-echo attenuation in a *q*-space plot, like that in Fig.1, should yield a curve that represents the distribution of dynamic displacements that arise from water diffusing in the restricted spaces of the RBC suspension. This distribution of $\bar{z}$ values is called the average propagator (see Eq. 3 below). While it is possible to directly apply a numerical Fourier transform to the data it turns out to be useful to enhance the usually featureless *q*-space plot; to this end we introduced a numerical procedure that is based on applying numerical

filtering and feature-enhancement via a *Mathematica* [23] program: (1) The 16-92 points (N) in a q-space data set (q_i, s_i) are interpolated with a shifting cubic-spline using the standard *Mathematica* function, **Interpolation**; (2) the interpolation function which is a smooth function of as many points as required (certainly many more than the original data set) is numerically differentiated, twice using the function **D**; (3) a Blackman-Harris bell-shaped filter ($\sin^4[\pi\ q_i/q_N]$) is then applied; and (4) then the data are numerically Fourier transformed by using the standard *Mathematica* function **Fourier**. With due attention given to the physical scales in the graphs, the signal for ^1H_2O in human RBCs yields a spectrum of mean displacements of the diffusing water [22]. A typical example is shown in Fig. 2.

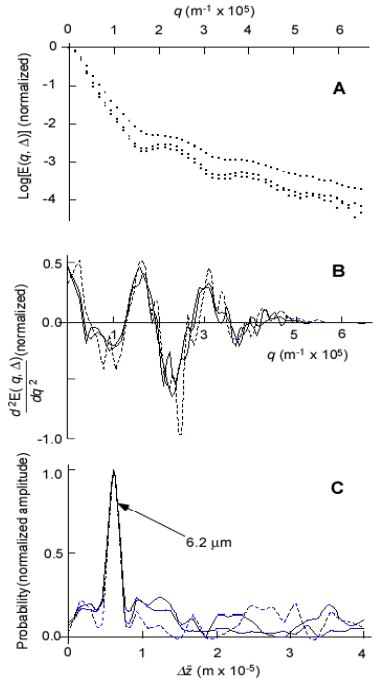

Fig. 2. PGSE NMR q-space plots of water diffusing in suspensions of human RBCs of three different packing densities (haematocrits; Ht). **A**, The logarithm of the signal attenuations versus q. **B**, The second derivatives of the data in **A**, that had been numerically interpolated with a shifting cubic-spline into the *non-logarithmic* version of the data. **C**, The data in **B** were multiplied by a Blackman-Harris filter and then Fourier transformed. The largest peak had an ordinate value that corresponded to a mean dynamic displacement of 6.2 μm.

Ht = 58% for upper row of dots and dashed lines in **B** and **C**; Ht = 48% for the central row of dots and the thin solid lines in **B** and **C**; and Ht = 40.8% for the bottom row of dots and thick solid lines in **B** and **C**. (Adapted from [22].)

Figure 2C shows that the main diffusion-restricting barriers (the cell membranes) have a spacing of 6.2 μm between them within a single cell; this is less than the known main diameter of 8 μm of the human RBC. The lower estimate arises because water-exchange across the membrane is rapid which decreases the apparent diameter of the cell; also each cell has a circular and not a rectangular cross-section [16].

The 'signatures' (special features) in q-space plots that are brought about by canonical forms of packing of biconcave RBCs has been extensively studied by using Monte Carlo computer simulations of restricted diffusion [24-26]. We conclude that, given the natural variations in RBC size and shape, the secondary features of q-space plots evident in these simulations, while distinct for ideal packing arrays, are unlikely to be interpreted

unambiguously in real samples. On the other hand for highly uniform geological samples this may be possible.

Monte Carlo methods are very powerful for simulating diffusion in systems of almost any conceivable arrangement of restrictions and obstructions [12,24-26]. However, it is still important to gain impressions of the shapes of *q*-space plots that would be obtained from canonical systems of diffusion-confining arrays for which there are analytical solutions to the relevant NMR-diffusion equations. We consider this matter next.

4. Fundamental q-Space Theory

The following theory explains how, with conventional PGSE NMR *q*-space experiments, the coherence features in the plots are simply related to the geometry of the diffusion-confining bodies in the sample [20,21,27]. The theory for spins that diffuse in the space(s) *outside* geometrically well-defined bodies is much less well developed and to date such analyses on cellular systems tend to have exploited Monte Carlo simulations [e.g., 11,16,24-26].

The theoretical treatment of restricted diffusion in PGSE NMR experiments [2,3] that yields most insights is the one in which the duration, δ, of the field gradient pulses is taken to be so short that spins do not move significantly during the pulses; this is called the short gradient pulse (SGP) approximation. In this situation the normalized spin-echo signal intensity $E[\mathbf{g}, \Delta]$ (in which the effects of relaxation during the experiment are cancelled out by normalizing the signal intensities to the one for which $\mathbf{g} = 0$) is described by the expression:

$$E[\mathbf{g}, \Delta] = \int \rho[\mathbf{r}_0 \mid \mathbf{r}, \Delta] \; exp[i \, \delta \, \mathbf{g} \cdot (\mathbf{r}_0 - \mathbf{r})] \, d\mathbf{r}_0 d\mathbf{r} \tag{1}$$

where $\rho[\mathbf{r}_0 \mid \mathbf{r}, \Delta]$ is the conditional probability density that describes the probability of a spin starting at the position $\mathbf{r}_0$ and ending at $\mathbf{r}$ in the time interval Δ; Δ is the time interval between the field gradient pulses of amplitude g in a specified direction hence it is a vector $\mathbf{g}$; and the vector $\mathbf{q} = (2\pi)^{-1} \gamma \, \delta \, \mathbf{g}$ describes a metric space that is the reciprocal of the space of displacement vectors $(\mathbf{r} - \mathbf{r}_0)$. To highlight this idea we write Eq. (1) with $\mathbf{R} = (\mathbf{r} - \mathbf{r}_0)$ to give,

$$E[\mathbf{q}, \Delta] = \iint \rho[\mathbf{r}_0] \, P[\mathbf{r}_0 \mid \mathbf{r}_0 + \mathbf{R}, \Delta] \; exp[i \, 2\pi \, \mathbf{q} \cdot \mathbf{R}] \, d\mathbf{r}_0 d\mathbf{R} \tag{2}$$

In the development of the whole area of SGP-*q*-space theory the 'key insight' was that of the average propagator [20,21]; it is the ensemble average probability density of the displacement vector $\mathbf{R}$ which is defined by,

$$\bar{P}[\mathbf{R}, \Delta] = \int \rho[\mathbf{r}_0] \, P[\mathbf{r}_0 \mid \mathbf{r}_0 + \mathbf{R}, \Delta] \, d\mathbf{r}_0 \tag{3}$$

Hence by substituting this expression into Eq (2) we obtain,

$$E[\mathbf{q}, \Delta] = \int \bar{P}[\mathbf{R}, \Delta] \; exp[i\, 2\, \pi\, \mathbf{q} \cdot \mathbf{R}]\, d\mathbf{R} \tag{4}$$

Equation (4) is the definition of the Fourier transform of $\bar{P}[\mathbf{R}, \Delta]$ where the variables in the conjugate spaces are **q** and **R**. Thus,

$$\bar{P}[\mathbf{R}, \Delta] = \int E[\mathbf{q}, \Delta] \; exp[-i\, 2\, \pi\, \mathbf{q} \cdot \mathbf{R}]\, d\mathbf{q} \tag{5}$$

When the time interval between the gradient pulses, Δ, is so large that each spin in a confined region 'maps out' the full extent of a restricting region, then its final position is independent of its starting position. Thus the sole determinant of the final position of each spin is the positional probability density $\rho[\mathbf{r}]$ of the compartment itself and it is not related to the value of the diffusion coefficient at all; thus Eq. (1) becomes:

$$E[\mathbf{q}, \infty] = \int \rho[\mathbf{r}_0]\, exp[i\, 2\, \pi\, \mathbf{q} \cdot \mathbf{r}_0]\, d\mathbf{r}_0 \int \rho[\mathbf{r}]\, exp[-i\, 2\, \pi\, \mathbf{q} \cdot \mathbf{r}]\, d\mathbf{r} \tag{6}$$

$$E[\mathbf{q}, \infty] = S^*[\mathbf{q}]\, S[\mathbf{q}] = |S[\mathbf{q}]|^2 \tag{7}$$

where $S[\mathbf{q}]$ is the counterpart of the conventional k-space NMR image expression [27]. The probability density $\rho[\mathbf{r}]$, for the situation in which there is a gradient only in the *z*-direction is merely the projection of the shape of the confining cavities onto the *z*-axis. Hence the approach to the mathematical analysis that is required is clear; derive the relevant *z*-projections of model compartments and perform the integrals in Eq. (6). We return to this more abstract phase of the paper after a practical aside.

5. Flow Diffraction

Artifacts can arise in NMR studies of cells due to their settling (possibly at a uniform rate) in the sensitive volume of the spectrometer probe. Thus the diffusion-diffraction effect could potentially be superimposed upon by a flow-diffraction effect [28-31]. To study this phenomenon and determine its likely influence in experiments on RBCs we built an apparatus that accurately measured the bulk flow on velocity scales that were of the order of only a few cell diameters per second.

In their work on NMR flow-diffraction Callaghan et al. [30,31] first investigated water flow in columns of packed glass and polymer spheres. They mathematically dissected out the contribution of flow from that of the self-diffusion 'pore-hopping' [14,15] in the spaces between the spheres that gives interference-like character to *q*-space plots; hence they estimated the mean diameter of the spheres by using this theory. They also generated convective flow in a capillary by exploiting the expansion of water that occurred over the length of the sample with a temperature difference of 4°C.

Both of these studies employed an experimental setup that was less direct than what we sought: We used a conventional laboratory peristaltic pump with a bubble trap and a long circuit of 6.5 m of Tygon tubing. This arrangement ensured dampening of any

pulsatile flow introduced by the pump. The tubing was passed down the bore of the NMR magnet, through the probe, and was threaded down the conduit that normally houses the heater coil. De-ionised water of total volume ~60 mL was circulated by the pump with a very stable flow rate. The volume-flow rate of the water was measured using a pre-weighed flask and by recording the volume delivered in 10, 20 and 33 min; thus from measurements of the diameter of the tube the linear flow velocity, a, was calculated.

Figure 3 shows *q*-space plots for three different flow rates. The diffraction-like features of the plots are obvious. The linear flow velocity was calculated from the NMR data as follows, and it was based on the assumption that the signal attenuation due to convection (coherent motion) was greatly in excess of that due to self-diffusion (incoherent motion); this is a realistic assumption given that the time over which the motion was measured was $\Delta = 40$ ms.

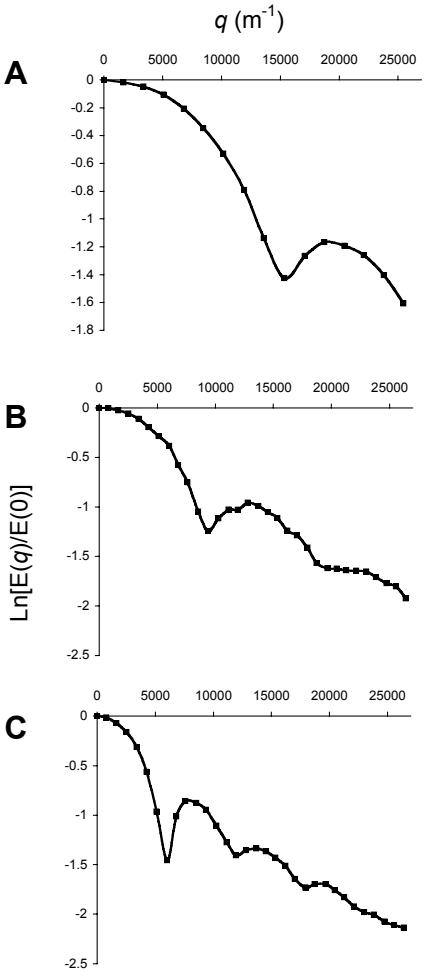

Fig. 3. Diffraction patterns evident in the *q*-space plots of the ^{1}H PFGSE NMR signal from flowing water. Water was pumped up through a high-gradient diffusion probe, in a vertical-bore 9.4 T NMR magnet in the direction of the main magnetic field and field gradients (i.e., *z*-gradients). A Gilson Minipuls II pump was used with 2.71 mm i.d. (color code: white/purple) Technicon pump tubing, and the flow-rate settings on the Vernier dial were: **A**, '20'; **B**, '50'; and **C**, '100'. Independent measurements of linear flow rates were made gravimetrically, using a tared vessel and timing the bulk flow coupled with the measured diameter of the Tygon tubing. The linear flow rates were (μm s^{-1}): **A**, 834; **B**, 1,320; and **C**, 2,150. The closed water-circuit was via 3.2 mm i.d. clear Tygon tubing, of total length 6.5 m; and a bubble trap was connected immediately after the pump; its total volume was ~2 mL and it contained ~1 mL of air as a 'dampener' of the pulsatile flow that the pump produced [32]. The tubing-circuit was not thermally regulated but the whole assembly was equilibrated within the temperature-controlled spectrometer room. The NMR spectrometer was a Bruker AMX 400 with an Oxford Instruments 9.4 T wide-bore magnet. A Bruker high-gradient diffusion probe (maximum ~10 T m^{-1}) with the gradient along the *z*-axis only, and carrying a ^{1}H exchangeable r.f.-coil insert, was used. The power-supply for the gradient coils was made by Bruker, and the gradient intensity was under software control (*uxnmr*). The pulse sequence was a conventional Carr-Purcell spin-echo with 16-step phase cycle; the field gradients were 4 ms in duration (δ) and separated by 40 ms (Δ); and 32 spectra were acquired for each *q*-space plot, each derived from summing 64 transients, with an inter-transient delay of 2.8 s.

6. Analysis of Flow-Diffraction Data

When the distance moved in a given observation time by a liquid flowing in a tube of uniform cross-section is constant across the diameter of the tube, the flow is defined as plug flow; NMR flow diffraction under these conditions, for which dispersion distances due to molecular diffusion are much less than the distances of the bulk flow, has already been thoroughly analyzed [28,29]. There have been few studies of flow-diffraction since these early reports, and yet it seemed worthwhile to explore some systems again using modern NMR instrumentation, new data processing methods, and in the context of NMR of cells.

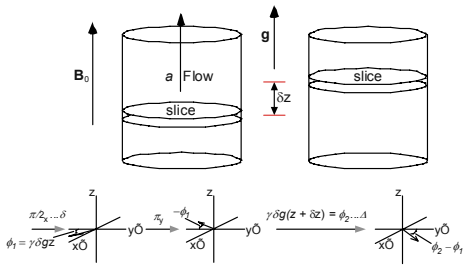

Fig. 4. Schematic representation of a virtual slice of thickness δz of flowing water in very slow lamina, or plug, flow, subjected to a PGSE experiment. The phase (ϕ) behaviour of the magnetization vector during the experiment is also shown. $\mathbf{B}_0$ is the main magnetic field; **g** is the magnetic field gradient vector; and *a* is the flow velocity.

The analysis of the data in Fig. 3 can be carried out in a very simple way with little recourse to complex mathematics. It relies on the assumption of plug flow, which as the results show by their consistency with gravitational measurements, pertained in these experiments: Consider a transverse slice of the cylindrical tube inside the sensitive volume of the NMR probe (Fig. 4). The first ($\pi/2_x$) radio frequency pulse in the PGSE experiment nutates the magnetization of the flowing water into the -*y*'-axis of the rotating frame. A few milliseconds later a magnetic field gradient pulse of duration δ seconds is applied. This advances the magnetization vector in the *x*',*y*'-plane. Thus the gradient pulse can be viewed as a *z*-axis pulse whose nutation angle is $\phi_1 = \gamma\, \delta\, g\, z$, where *z* is the axial coordinate in the sample. Next the π_y pulse rotates the magnetization vector about the -*y*'-axis thus bringing about a phase retardation of $-\phi_1$; and the second field-gradient pulse, applied Δ seconds after the first, again invokes a phase change of $\phi = \gamma\, \delta\, g\, (z + \delta z)$, where δz is the distance moved by the transverse 'slice' of water in the time Δ between the two gradient pulses. The sum of the phase changes imparted by the two gradient pulses, noting the minus sign introduced by the π_y RF pulse on $-\phi_1$, is simply $\Delta\phi = \gamma\, \delta\, g\, \delta z$.

Since the uniform linear flow-velocity is *a* m s^{-1} then $a = \delta z/\Delta$; and by definition $\mathbf{q} = (1/2\pi)\, \gamma\, \delta\, \mathbf{g}$ so the change in phase angle brought about by flow is:

$$\Delta\phi = 2\, \pi\, q\, \delta z = 2\, \pi\, q\, a\, \Delta \qquad (8)$$

The amplitude of the spin-echo signal is described by a squared sinc function of the phase angle $\Delta\phi$ [28,29]; this is exactly analogous to how the intensity of a light band in an optical diffraction pattern varies as the square of the sinc function of the displacement

angle of the band relative to the undeviated path of light from a rectangular slit [18]. Hence, the normalized signal $S[q, \Delta]$ is proportional to,

$$S[q, \Delta] \propto \sin^2[2 \pi q a \Delta]/(2 \pi q a \Delta)^2 \quad (9)$$

This function is periodic in q and has minima when the argument is an integer multiple of π, *viz*.,

$$q_{\min,n} = n/(2 a \Delta) \quad (10)$$

Therefore, experimentally the linear-flow velocity a is estimated from,

$$a = n/(2 q_{\min,n} \Delta) \quad (11)$$

In Fig. 3A the first (and only) minimum in the curve is at $q_{\min,1} = 1.54 \times 10^4$ m^{-1}, and using $\Delta = 0.04$ s this yields via Eq. (11) a flow-velocity estimate of 8.12×10^{-4} m s^{-1}; this value compared well with the gravimetrically-determined value of 8. 34×10^{-4} m s^{-1}. In Fig. 3B the minima are at $q_{\min,1} = 0.94 \times 10^4$ m^{-1} and $q_{\min,2} = 1.97 \times 10^4$ m^{-1} which corresponds to $a = 1.33 \times 10^{-3}$ m s^{-1} and 1.27×10^{-3} m s^{-1}, respectively, which also compared well with the gravimetric estimate of 1.32×10^{-3} m s^{-1}. Finally, the three flow-diffraction minima in Fig. 3C yielded estimates of a of 2.10×10^{-3} m s^{-1}, 2.10×10^{-3} m s^{-1}, and 2.09×10^{-5} m s^{-1}, respectively, that were very similar to the gravimetric estimate of 2.15×10^{-3} m s^{-1}.

In conclusion, a simple experimental arrangement was shown to be amenable to the measurement of slow lamina-plug flow rates, using q-space analysis. The results give insight into those rates of cell sedimentation that might distort the diffusion-diffraction q-space plots obtained from suspensions of RBCs. Our experience with human RBCs suggests that the avoidance of cell settling is easily achieved by using haematocrits greater than 65%; and there does not appear to have been any evidence in our previous work of a settling artifact in the analysis of RBC shapes [11,12,16]. In addition our experimental arrangement is suitable for work with flowing cells.

7. Model of Cellular Arrays

There is interest in defining a system of ordered prisms that might serve as a plausible representation of an array of cells in a suspension or a tissue; the ordered columns of cells around the central sinusoid in the mammalian liver is particularly striking in this regard. By using a model in which dimensions of compartments (a) were such that the diffusion distance for water molecules at room- or body-temperature would make $a^2/(\Delta D) << 1$ in a PGSE experiment, then the theory in Section 4 can be applied. If the system were well chosen, analytical expressions for the integrals in Eq. (6) might be obtained. Thus q-space plots could be predicted based on the basis of the geometry of the array. We defined an array of cells in such a way that a single adjustable parameter determines the packing density (haematocrit) of the cells. The system was built upon a 2-dimensional square tessellation (crystallographic space group P1) with each cell represented by a block of

four squares (side length a/2); and with each outer corner able to be moved symmetrically, equally, and radially toward the centre of the block. The extent of this movement determines the relative area and hence volume of the 'extracellular' space. Since this is a 2-dimensional array, the columns of cells are taken to be effectively unbounded in the direction orthogonal to $\mathbf{B}_0$. While the columns are unbounded they can be conceived of as having transverse partitions that represent membranes, without affecting the present theory.

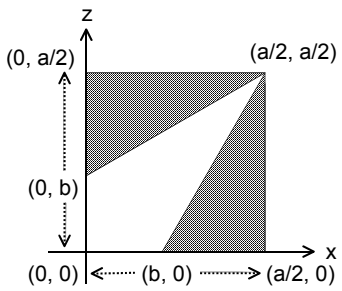

Fig. 5. Construction element of the octagon-star array of prisms that serve as a model of an ordered biological tissue shown in Figs 6D-F. For simulating q-space diffusion experiments the direction of $\mathbf{B}_0$ was taken to be along the z-axis. The square that forms the basis of the array of octagons and interstitial stars has side-length $a/2$; thus the block of four squares has length a; the two lines that define the sides of the four-pointed star intersect at ($a/2$, $a/2$) and respectively cut the x- and z-axes at (b, 0) and (0, b). Note that $b < a/2$. In the limit as $b \rightarrow 0$ the octagon-array becomes a square tessellation parallel to the x- and z-axes (Fig. 6F); while as $b \rightarrow a/2$ the array is at 45° to the axes (Fig. 6D). For Figs 6A-C the construction element was rotated by 45°.

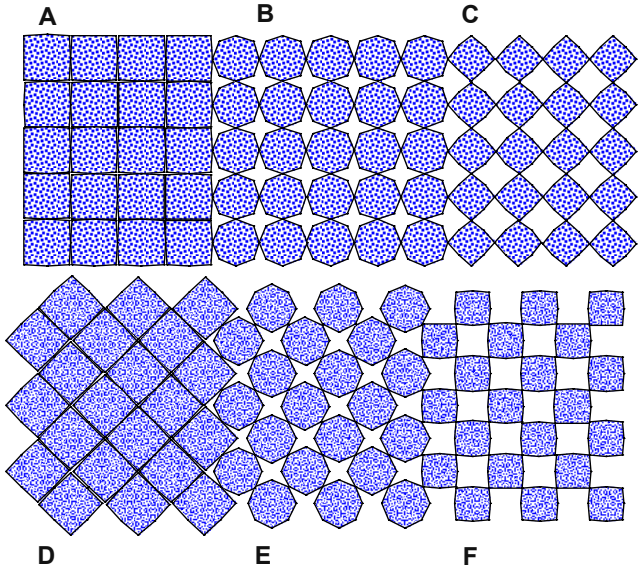

Fig. 6. Canonical, octagon-star arrays used to explore the range of forms of q-space plots that might be obtained from highly ordered biological tissues, or inanimate materials such as zeolites. **A-C**, the array orientated with the two diametrically opposite points of each star aligned with the x- and z-axes; **D-F**, the array rotated by 45°. The direction of $\mathbf{B}_0$ was taken to be vertically up the page along the z-axis.

8. Analytical q-Space Solutions

The simulation of PGSE NMR *q*-space plots that would be obtained from samples arranged with diffusion restricting barriers (e.g., cell membranes) like those in Fig. 6 is achieved with solutions of Eq. (6). We suppose that the magnetic field gradients occur only along the *z*-direction so we seek an expression for the probability density $\rho(z)$ of points from an octagon, and a star projected onto the *z*-axis. The solution involves the set of integrals that are taken between the straight line segments that define the regions shown in Fig. 5; and we use Euler's formula to express the exponentials in Eq. (6) as the relevant trigonometric functions. The PGSE signal as a function of **q** is Eq. (7) written in terms of the integrals whose subscripts denote the relevant regions:

$$E[\mathbf{q},\infty]_{total} = I_{star,+}I_{star,-} + I_{octagon,+}I_{octagon,-} \tag{12}$$

The sub-expression for the star shape in Fig. 6D-F is,

$$I_{star,\pm} = \int_0^b \left(b + z - \frac{2\,b\,z}{a}\right) Cos[2\,\pi\,q\,z]\,dz + i\int_0^b \left(b + z - \frac{2\,b\,z}{a}\right) Sin[2\,\pi\,q\,z]\,dz \pm$$
$$\int_b^{a/2} 2\left(\frac{b(a-b)(a-2\,z)}{a(a-2\,b)}\right) Cos[2\,\pi\,q\,z]\,dz + i\int_b^{a/2} 2\left(\frac{b(a-b)(a-2\,z)}{a(a-2\,b)}\right) Sin[2\,\pi\,q\,z]\,dz \tag{13}$$

and for the octagon it is,

$$I_{octagon,\pm} = \int_b^{a/2} a\left(\frac{z-b}{a-2\,b}\right) Cos[2\,\pi\,q\,z]\,dz + i\int_b^{a/2} a\left(\frac{z-b}{a-2\,b}\right) Sin[2\,\pi\,q\,z]\,dz \pm$$
$$\int_{a/2}^{a} \left(b + z - \frac{2\,b\,z}{a}\right) Cos[2\,\pi\,q\,z]\,dz + i\int_{a/2}^{a} \left(b + z - \frac{2\,b\,z}{a}\right) Sin[2\,\pi\,q\,z]\,dz \tag{14}$$

noting that the haematocrit that we can vary and thus change the form of $E[\mathbf{q}, \Delta]$ is given by:

$$Ht = \left(1 - \frac{b}{a}\right) \quad b < \frac{a}{2} \tag{15}$$

The integrals in Eqs (14) and (15) are not intrinsically difficult to solve but the task is extremely tedious to do 'by hand'. Thankfully, they are readily solved symbolically (analytically) by using the function Integrate in *Mathematica* [23]. To convey an impression of the complexity of the expressions that arise from the analysis, that for the signal from the stars in Fig. 6D-F is given by:

$$E_{star}[q,\infty]=\frac{1}{8a^2(a-2b)^2\pi^4q^4}\times$$
$$\left(\begin{array}{l} a^4-4a^3b+20a^2b^2-32ab^3+16b^4+2a^2(a-2b)^2b^2\pi^2q^2-a^2(a-2b)^2\mathrm{Cos}[2b\pi q]+ \\ 4(a-b)b\left((a-2b)^2\mathrm{Cos}[a\pi q]-a\left(a\mathrm{Cos}[(a-2b)\pi q]+2(a-2b)b\pi q\mathrm{Sin}[a\pi q]\right)\right)+ \\ 2a^3(a-2b)b\pi q\mathrm{Sin}[2b\pi q] \end{array}\right) \tag{16}$$

In the interests of conserving space the other expressions are not given here but they can be obtained from the corresponding author. While it is possible to derive satisfaction from writing an analytical solution to the problem, in practice the mathematics only becomes useful when it is coupled with a convenient means of rapid evaluation and graphical output. Accordingly we simulated and graphed the behaviour of restricted diffusion of a molecule like water by varying both q and Ht using the 3-dimensional graphics function ListPlot3D in *Mathematica* (e.g., as in [33]).

Figure 7 shows the dependence of the normalized spin-echo signal intensity $E[q, \infty]$ from a PGSE NMR experiment, that would be obtained from water diffusing in an array of cells that have an octagonal cross-section with the main diameter similar to that of a typical cell, 10 μm. The range of q was chosen to be the same as used in many real experiments (see Figs 1 and 2) on RBCs, *viz*., 0 - 10^6 (m^{-1}). It is clearly seen in Fig. 7A that as Ht is increased, making the interstitial space smaller and the star shape more pointed, that the features of the diffraction pattern become better defined. This is in contrast to the situation in Fig. 7C which shows the opposite effect. Another, underlying difference is that the array has been rotated through 45° with respect to $\mathbf{B}_0$ thus producing the marked change in the features of the diffraction surface.

Figures 7B and D are views from a different perspective of the surfaces; these give a better impression of the form of the q-space plot when Ht = 100%. Thus another feature is apparent: the number of lobes in Fig. 7D at Ht = 100% is greater than in Fig. 7B. This comes about because the maximum projection of an octagon onto the z-axis in the former is greater than for the latter; and since q defines a *reciprocal*-distance space the q-period is less. This is also apparent, but less clearly, for Ht = 0 in Figs 7A and C.

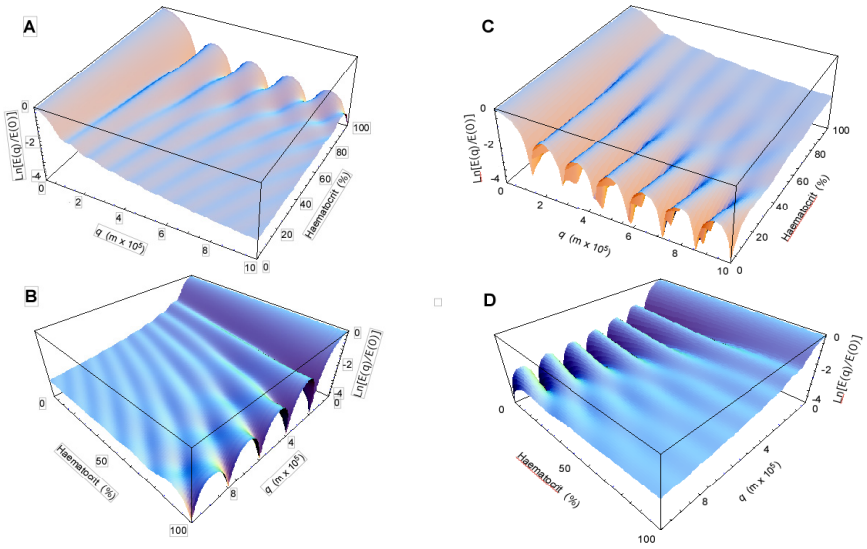

Fig. 7. *q*-Space plots calculated for the octagon-star arrays in Fig. 6, for a range of packing densities (haematocrits; *Ht*) of the octagons shown in Fig. 6. For the series in the array in Figs 6D-F where $\mathbf{B}_0$ was assumed to be parallel to the axis between pairs of points of each star, **A** is the view of the three-dimensional surface from the side where *Ht* = 0%; **B**, from the side where *Ht* = 100%. For the series in Fig. 6A-C, **C** is the view of the three-dimensional surface from the side where *Ht* = 0%; **D**, from the side where *Ht* =100%. The calculations were made with *Mathematica*.

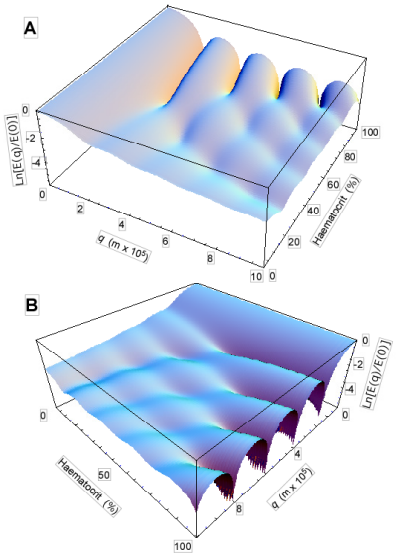

Fig. 8. Simulated *q*-space surfaces obtained for a range of packing densities (haematocrits; *Ht*) of the stars alone, as in Fig. 6D-F, assuming no NMR signals emerge from the octagons. When *Ht* = 0 the star is a square with one of the main diagonals along the direction of $\mathbf{B}_0$; when *Ht* is just < 100% each star is a cross with sharp points, so in a real experiment the signal would be very weak compared with the case when *Ht* is a smaller value.

Figure 8 shows the form of the *q*-space surface for the situation in which signal is only from the star-shaped compartments; this is the analogue of the intercellular space in our model. Such a plot could come about in real systems when a membrane-impermeant labeled solute is used in the experiment. Note the dimples in the surface between the two sets of intersecting spatial waves. These and their positions are related to the interplay between the projections of the points of the stars and that of its central body. Further insight into the origins of the features could come about by studying the star-shape alone and varying the relative proportions or each feature, unconstrained by the presence of the octagons.

9. Conclusions

We have reviewed the state-of-the-art with respect to the resolution of features in PGSE NMR *q*-space plots that are obtained from suspensions of fresh human RBCs. The signal-to-noise ratio available in a modern NMR spectrometer operating at or above 400 MHz for protons, and equipped with a commercial pulsed-field-gradient probe should reproducibly yield results like those in Fig. 1, in ~30 – 60 min. The application of feature-enhancement strategies like that used for Fig. 2 appear to be a valuable tool for tracking changes of cell shape, such as with the discocyte-echinocyte-spherocyte transition that occurs over a time course of several hours. However, in order to 'catch' a time course of the shorter time scale of the first part of this transition, some of the newer fast-DOSY experiments will need to be employed, or specialized versions developed (see our paper on pages 52-68).

The short gradient pulse (SGP) theory of the *q*-space experiment is valuable in conveying an understanding that has close analogies with diffraction and interference effects in physical optics, that have been extensively analyzed [e.g.,18]. The ability to obtain analytical solutions to the master equation in this theory (Eq. 6) by using *Mathematica* (and presumably similar programs like Maple) means that impressions of the factors that characterize the forms of *q*-space plots can be gleaned by repeated simulations. Overall though, we are pessimistic that truly unique signatures in *q*-space plots will ever be able to be found that will define underlying cell shapes or packing arrangements. In other words, the inverse problem does not appear to have a unique solution, at least given the current signal-to-noise ratios that are available in the standard PGSE NMR experiment. On the other hand, with human RBCs there are very clear differences in the *q*-space plots from discocytes and spherocytes [11,12]; and this has already been of some practical experimental utility. Also, curves like Fig. 1 routinely yield robust estimates of the main diameter of the RBCs. What is unique about this result is that the cell diameter is measured at high packing densities, in contrast to light microscopy in which clear delineation of cells requires packing densities < 1%. Such low packing densities obtained by dilution in buffers are often accompanied by artifacts due changes in osmolality, and contact between the RBCs and the charged surface of the microscope slide that induce shape changes.

The flow-diffraction analysis that we present is applicable only to plug flow. The complete theory has been presented elsewhere; it addresses the paraboloidal flow-front

that is well known for fluids in non-turbulent, Poiseuille flow [28,29]. However, our data reveal the high quality of flow-diffraction data that are available with our simple apparatus in a modern NMR spectrometer. The main conclusion relevant to the studies on cells is that flow-diffraction is not a significant source of error in *q*-space analysis of RBCs in suspensions where *Ht* is > ~65%, or, of course, if the densities of the medium and the cells are matched.

Finally, PGSE NMR *q*-space analysis provides another window into microscopic systems that contain uniform repeated structures; and it is most informative in cases where the underlying restricting barriers are of the same size (like RBCs) so periodicities in the *q*-space plots become well defined. Then the data can be image-enhanced and a robust representation of the average propagator obtained. Future developments in this area will probably be in more rapid acquisition of *q*-space plots to study systems that are rapidly evolving.

Acknowledgements

The work was supported by a Discovery Grant from the Australian Research Council to PWK. Dr Bob Chapman is thanked for contributions to the experiments for Fig. 3 and for his long-term participation in the NMR work of our group.

References

[1] P. J. Mulquiney, P. W. Kuchel, Modelling Metabolism with *Mathematica*, CRC Press, Boca Raton, FL, 2003.
[2] E. O. Stejskal, J. E. Tanner, J. Chem. Phys. 42 (1965) 288-292.
[3] E. O. Stejskal, J. Chem. Phys. 43 (1965) 3597-292.
[4] J. Kärger, Ann. Phys. 24 (1969) 1.
[5] J. Kärger, Ann. Phys. 27 (1969) 107.
[6] A. R. Waldeck, M. H. Nouri-Sorkhabi, D. R. Sullivan, P. W. Kuchel, Biophys. Chem. 55 (1995) 197-208.
[7] W. S. Price, B. E. Chapman, B. A. Cornell, P. W. Kuchel, J. Magn. Reson. 83 (1989) 160-166.
[8] W. S. Price, P. W. Kuchel, B. A. Cornell, Biophys. Chem. 33 (1989) 205-215.
[9] P. W. Kuchel, B. E. Chapman, J. Magn. Reson. 94 (1991) 574-580.
[10] A. R. Waldeck, P. W. Kuchel, A. J. Lennon, B. E. Chapman, Progr. NMR Spectrosc. 30 (1997) 39-68.
[11] A. M. Torres, R. J. Michniewicz, B. E. Chapman, G. A. R.Young, P. W. Kuchel, Magn. Reson. Imag. 16 (1998) 423-434.
[12] A. M. Torres, A. T. Taurins, D. G. Regan, B. E. Chapman, P. W. Kuchel, J. Magn. Reson. 138 (1999) 135-143.
[13] D. G. Cory, A. N. Garroway, Magn. Reson. Med. 14 (1990) 435-444.
[14] P. T. Callaghan, A. Coy, D. McGowan, K. J. Packer, F. O. Zelaya, Nature 351 (1991) 467-469.
[15] P. T. Callaghan, A. Coy, T. P. J. Halpin, D. McGowan, K. J. Packer, F. O. Zelaya, J. Chem. Phys. 97 (1992) 651-662.
[16] D. G. Regan, P. W. Kuchel, Israel J. Chem. 43 (2003) 45-54.
[17] P. W. Kuchel, A. Coy. P. Stilbs, Magn. Reson. Med. 37 (1997) 637-643.

[18] F. A. Jenkins, H. E. White, Fundamentals of Optics, McGraw-Hill, New York, 3rd Edn, pp 288-310,1975.
[19] P. W. Kuchel, C. D. Durrant, P. S. Jarrett, D. G. Regan, J. Magn. Reson. 145 (2000) 291-301.
[20] J. Kärger, W. Heink, J. Magn. Reson. 51 (1983) 1-7.
[21] J. Kärger, H. Pfeifer, W. Heink, Adv. Magn. Reson. 51 (1988) 1-89.
[22] P. W. Kuchel, T. Eykyn, D. G. Regan, Magn. Reson. Med. 52 (2004) 907-912.
[23] S. Wolfram, The *Mathematica* Book, Wolfram Reseach, Champaign, IL (2005).

[24] D. G. Regan, P. W. Kuchel, Eur. Biophys. J. 29 (2000) 221-227.
[25] D. G. Regan, P. W. Kuchel, Biophys. J. 83 (2002) 161-171.
[26] D. G. Regan, P. W. Kuchel, Eur. Biophys. J. 31 (2003) 563-574.
[27] P. T. Callaghan, Principles of Nuclear Magnetic Resonance Microscopy, Oxford University Press, Oxford (2003).
[28] K. J. Packer, Mol. Phys. 17 (1969) 355-368.
[29] R. J. Hayward, K. J. Packer, D. J. Tomlinson, Mol. Phys. 23 (1972) 1083-1102.
[30] J. D. Seymour, P. T. Callaghan, J. Magn. Reson. A 122 (1996) 90-93.
[31] B. Manz, J. D. Seymur, P. T. Callaghan, J. Magn. Reson. 125 (1997) 153-158.
[32] P. Lundberg, S. Roy, P. W. Kuchel, J. Immunometh. 4 (1994) 163-178.
[33] P. W. Kuchel, C. J. Durrant, J. Magn. Reson. 139 (1999) 258-272.